Journal of Materials Chemistry C

PAPER

View Article Online
View Journal | View Issue

Cite this: J. Mater. Chem. C, 2019, 7, 6289

Influence of composition and structure on the thermal quenching of the 5d–4f emission of Eu^{2+} doped M–Si–N (M = alkali, alkaline earth, rare earth) nitridosilicates†

Otmar M. ten Kate, *[a] J. Ruud van Ommen [a] and H. T. (Bert) Hintzen[b]

Experimental data from literature on the thermal quenching of the Eu^{2+} 5d–4f emission in the $M_xSi_yN_z$ (M = alkali, alkaline earth or rare earth) nitridosilicates have been collected and evaluated. No clear correlation was observed between the activation energy for thermal quenching and the Stokes shift, suggesting that non-radiative relaxation *via* a thermally excited cross-over from the 5d excited state to the 4f ground state is not the main reason for thermal quenching in the nitridosilicates. Based on literature data on rare-earth charge transfer transitions, host-lattice bandgap and Eu^{2+} 5d–4f emission energy, the energy difference between the Eu^{2+} 5d level and the bottom of the host-lattice conduction band has been determined. This energy difference correlates fairly well with the quenching temperature, suggesting that thermal ionization of the 5d electron to the conduction band is responsible for the thermal quenching of the Eu^{2+} 5d–4f emission in the nitridosilicates. The energy difference between the lowest 5d level and the bottom of the conduction band, and consequently the quenching temperature, increases with increasing Si/N ratio of the nitridosilicates. From this, it is concluded that the combined effect of the larger Stokes shift and the raise in energy of the bottom of the host lattice conduction band with increasing Si/N ratio is stronger than the decrease of the centroid shift and crystal field splitting of the Eu^{2+} 5d level.

Received 16th March 2019,
Accepted 27th April 2019

DOI: 10.1039/c9tc01445d

rsc.li/materials-c

1. Introduction

Phosphor-converted white light-emitting diodes (pc-wLEDs) have attracted significant attention in recent years as they are considered an environmental friendly, cost-effective and energy efficient way to generate white light.[1–4] The first efficient pc-wLEDs, based on a blue LED chip and the yellow YAG:Ce^{3+} phosphor, still had a relatively poor colour rendering, as the white light from the LED missed a red component. Alternative approaches have therefore been the main interest of research and development, where a blue or UV LED chip is combined with a combination of (blue) red and green phosphors, leading to white light with a much better colour rendering.

An important class of phosphors for these high colour rendering pc-wLEDs, are the Eu^{2+} doped nitridosilicates.[5] These phosphors have the general composition $M_xSi_yN_z:Eu^{2+}$, where M can be an alkali, alkaline earth or rare-earth metal. Some of these nitridosilicate phosphors can very efficiently convert the UV or blue excitation light into longer wavelengths. Moreover, many of them are chemically stable in air (in particular those with low M/Si ratios) and the wide range of nitridosilicate structures, arising from the variety in Si/N ratios, allows for a large range of emission colours. Examples are blue-emitting $SrSi_6N_8:Eu^{2+}$,[6] green-emitting $LaSi_3N_5:Eu^{2+}$,[7] yellow-emitting $SrYSi_4N_7:Eu^{2+}$,[8] and red-emitting $SrSiN_2:Eu^{2+}$.[9] The red-emitting $Sr_2Si_5N_8:Eu^{2+}$ phosphor has been commercially applied as an LED phosphor. As an extension to the Eu^{2+} doped nitridosilicates, silicon can be partially substituted by aluminium and nitrogen by oxygen, leading to the even wider class of sialon phosphors. Well-known examples hereof are $CaAlSiN_3:Eu^{2+}$,[10] $(AE)Si_2O_2N_2:Eu^{2+}$ (AE = Ca, Sr, Ba),[11] Ca-α-sialon:Eu^{2+},[12,13] and β-sialon:Eu^{2+}.[14]

A very important property for LED phosphors, affecting the performance of in particular high-power LEDs, is the temperature dependency of the emission intensity. It is well known that with increasing temperature, the luminescence efficiency of the phosphors generally tends to decrease. This is especially a drawback for pc-wLEDs containing multiple phosphors, as it will not only decrease the light output, but will also change the overall colour emitted by the LED. Various strategies have therefore been

[a] Product and Process Engineering, Chemical Engineering, Applied Sciences, Delft University of Technology, Van der Maasweg 9, 2629 HZ Delft, The Netherlands. E-mail: o.m.tenkate@tudelft.nl
[b] Luminescent Materials Group, Radiation Science and Technology, Applied Sciences, Delft University of Technology, Mekelweg 15, 2629 JB Delft, The Netherlands

† Electronic supplementary information (ESI) available. See DOI: 10.1039/c9tc01445d

developed to obtain thermally stable LED phosphors,[15] like for the blue-emitting $Na_3Sc_2(PO_4)_3:Eu^{2+}$ phosphor that does not have any decrease of emission intensity up to 200 °C.[16] As for the (oxy)-nitride phosphors, the commercially available $Sr_2Si_5N_8:Eu^{2+}$, β-sialon:Eu^{2+}, $CaAlSiN_3:Eu^{2+}$ and $SrSi_2O_2N_2:Eu^{2+}$ phosphors show relatively good thermal stability, while for many other phosphors the emission intensity rapidly decreases with temperature.

The decrease of luminescence intensity with temperature can have two principally different reasons:[17] (1) by a degradation of the phosphor at higher temperature often caused by a reaction with water or oxygen, or (2) by thermal quenching of the luminescence. The first one is a permanent decrease of the luminescence, even if the phosphor is cooled down again, and depends on the (thermo-)chemical stability of the phosphor; the second one, the thermal quenching, is not permanent as the initial intensity restores when cooling down the phosphor. In this manuscript we will focus on this thermal quenching, with specific attention to the influence of composition and structure.

Various mechanisms have been proposed in literature that can be the origin of the thermal quenching of the Eu^{2+} 5d–4f emission. The two main ones are: (1) direct radiationless relaxation from the 5d excited state to the 4f ground state *via* a thermally activated cross-over,[18,19] and (2) thermal ionization by excitation of an Eu^{2+} electron from the 5d level to the conduction band.[20] In literature, both these models have been used to explain the differences in thermal quenching behaviour of the Eu^{2+} 5d–4f emission for the nitridosilicates. Thermal quenching *via* a thermally activated cross-over was considered by for example Fukuda,[21] who concluded that the thermal quenching in various Eu^{2+} doped Sr-containing sialon phosphors is influenced by the phonon frequency. On the other hand, thermal quenching *via* thermal ionization to the conduction band was, for example, considered by Tolhurst *et al.*,[22] using X-ray absorption spectroscopy to show that the lowest Eu^{2+} 5d level is closer to the bottom of the conduction band in $SrMg_3SiN_4:Eu^{2+}$ than in $Li_2Ca_2Mg_2Si_2N_6:Eu^{2+}$, explaining the stronger thermal quenching for $SrMg_3SiN_4:Eu^{2+}$ as compared to $Li_2Ca_2Mg_2Si_2N_6:Eu^{2+}$. The thermal quenching of Ce^{3+} and Eu^{2+} doped oxide and nitride phosphors has been reviewed recently by Wang *et al.*,[23] discussing various strategies to obtain phosphors with high thermal stability. In addition, Yan[24] recently reviewed and explained the causes of the shift of the Eu^{2+} and Ce^{3+} emission maxima with temperature for many different phosphors, including various nitridosilicates.

Recently, we have shown that the degree of condensation, expressed by the Si/N ratio, acts as a principle parameter that determines the coordination number of N with Si (NSi_x), the Si–N and M–N bond lengths and bandgap of the $M_xSi_yN_z$ nitridosilicates,[25] as well as the energy of the Eu^{2+} 4f–5d absorption and 5d–4f emission in the Eu^{2+} doped nitridosilicates.[26] The dependence on the Si/N ratio was explained by considering that with increasing Si/N ratio the coordination number of N with Si increases, which results in more N electrons that participate in the bonding with Si and consequently less N electrons that are available for M–N bonding. This makes the M–N bonds longer and less covalent, while the Si–N bonds become shorter, consequently resulting in a wider bandgap of the nitridosilicates.[25] The less covalent and longer Eu–N bonds for higher Si/N ratio also result in an increase of the Eu^{2+} 4f–5d absorption and 5d–4f emission energy due to a weaker nephelauxetic effect and a smaller crystal field splitting. The Stokes shift becomes larger with increasing Si/N ratio as the local rigidity of the site on which Eu^{2+} is located, decreases due to the longer Eu–N bonds.[26]

In this work we will extend this model by studying the effect of the Si/N ratio on the thermal quenching of the Eu^{2+} 5d–4f emission of the Eu^{2+} doped nitridosilicates. First, in Section 2, the two main mechanisms are discussed that have been proposed in literature as responsible for the thermal quenching of the Eu^{2+} 5d–4f emission. In Section 3, we summarize and evaluate data from literature on the thermal quenching of the Eu^{2+} 5d–4f emission in the nitridosilicates and determine the activation energy for thermal quenching as well as the quenching temperature. In Section 4 we evaluate and discuss the correlation between the quenching temperature and the degree of condensation (Si/N ratio) for the nitridosilicates, and show that this correlation can best be explained with the thermal ionization model.

2. Mechanisms of the thermal quenching of the Eu^{2+} 5d–4f emission

In literature, different mechanisms have been proposed that may be responsible for the decrease of Eu^{2+} 5d–4f emission intensity with increasing temperature. The main ones are: (1) thermally activated non-radiative relaxation from the Eu^{2+} 5d excited state to the 4f ground state *via* the crossing point of the 5d and 4f parabola, and (2) thermal ionization of the Eu^{2+} 5d electron to the host lattice conduction band. These mechanisms will be briefly discussed in Sections 2.1 and 2.2, respectively. In Section 2.3 other factors will be discussed that may influence the temperature dependency of the emission intensity.

2.1 Thermal quenching by direct radiationless relaxation to the ground state

One of the first mechanisms proposed in literature that can be the cause of the thermal quenching of the Eu^{2+} 5d–4f emission, is the direct relaxation from the 5d excited state to the 4f ground state *via* a thermally activated cross-over.[18,19,27] This mechanism can be described using a quantum mechanical single configurational coordinate (QMSCC) model, illustrated with the configurational coordinate diagram in Fig. 1a. After excitation of an Eu^{2+} electron from the 4f ground state to the 5d excited states, relaxation to the lowest 5d level will occur. From here 5d–4f emission can take place. According to the Franck–Condon principle these electronic transitions are vertical because the electronic transitions are much faster than any change in positions of the atomic nuclei. As an alternative to 5d–4f emission, the crossing point between the 4f and the 5d parabola may be reached if the thermal energy is higher than the energy difference between the minimum of the 5d parabola and the crossing point with the 4f ground state parabola, resulting in a non-radiative return from the 5d excited state

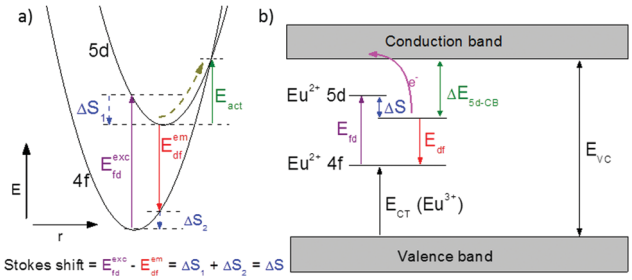

Fig. 1 (a) Configurational coordinate diagram of the 4f and 5d state of Eu^{2+}, with energy *E versus* configurational coordinate *r*, showing the mechanism of thermal quenching of the Eu^{2+} 5d–4f emission *via* the crossing point between the 5d and 4f parabola; (b) mechanism of thermal quenching of the Eu^{2+} 5d–4f emission by thermal ionization of the Eu^{2+} 5d electron to the host lattice conduction band, with energy difference $\Delta E_{5d\text{-}CB}$ between the relaxed 5d state and the bottom of the conduction band.

to the 4f ground state and thus thermal quenching of the 5d–4f emission. In this model, the 4f and 5d parabolas can be described with eqn (1) and (2) respectively:[28]

$$E_{4f} = \frac{1}{2}k_{4f}r^2 \quad (1)$$

$$E_{5d} = E_0 + \frac{1}{2}k_{5d}(r - r_0)^2 \quad (2)$$

Here are E_{4f}, k_{4f}, E_{5d} and k_{5d} the energy and force constant of the 4f and 5d parabolas respectively. r is the configurational coordinate (which can be represented by the Eu to coordinating anion distance), r_0 is the Frank–Condon offset between the two parabolas and E_0 is the energy difference between the minima of the 4f and the 5d parabolas. The activation energy (E_{act}) for the thermal quenching is equal to the energy difference between the minimum of the 5d parabola and the crossing point between the two parabolas. If the two parabolas have the same curvature with force constant k, it follows from eqn (1) and (2) that the activation energy is given by:

$$E_{act} = \frac{(2E_0 - kr_0^2)^2}{8kr_0^2} = \frac{(E_{df})^2}{2\Delta S} \quad (3)$$

Here is E_{df} the 5d–4f emission energy and ΔS the Stokes shift. If the Stokes shift becomes larger, *i.e.* when the offset between the 4f and 5d parabolas increases, the crossing point decreases in energy. So in this case, the activation energy for thermal quenching should decrease with increasing Stokes shift. Since the offset between the 4f and 5d parabola is related to the local[26] rigidity, the temperature dependency of the luminescence will in this model also depend on the rigidity.

2.2 Thermal quenching by thermal ionization to the host lattice conduction band

Another mechanism considered in literature to be responsible for the quenching of the Eu^{2+} 5d–4f emission, is the thermal ionization of the Eu^{2+} 5d electron to the host lattice conduction band,[20,29] illustrated in Fig. 1b. If the lowest 5d state is relatively close to the bottom of the conduction band, there is only a small energy barrier to overcome in order to bring the electron from the 5d state into the conduction band. Once this ionization has occurred, the return to the ground state of Eu^{2+} occurs non-radiatively, hence the Eu^{2+} 5d–4f emission is quenched. In the case of thermal ionization, the activation energy for thermal quenching will depend on the energy difference between the lowest relaxed (since the relaxation is much faster than the thermal ionization) Eu^{2+} 5d state and the bottom of the host-lattice conduction band. If the energy difference is large, the energy barrier for thermal quenching will also be large, and *vice versa*. If the lowest relaxed 5d state is located inside the conduction band, auto-ionization may occur even at low temperature, and the emission will be completely quenched.[30]

The energy difference between the lowest non-relaxed 5d state and the bottom of the host lattice conduction band is, by definition, equal to the bandgap minus the Eu^{2+} 4f–5d absorption energy and minus the energy between the top of the host lattice valence band and the Eu^{2+} 4f ground state,[20] as illustrated in Fig. 1b. The energy between the top of the valence band and the Eu^{2+} 4f ground state equals the Eu^{3+} charge transfer (CT) energy, for the transfer of an electron from a coordinating anion to Eu^{3+}.[31] In order to obtain the energy difference $\Delta E_{5d\text{-}CB}$ between the lowest relaxed 5d state and the bottom of the conduction band, the energy for relaxation needs to be taken into account, which can be approximated by the Stokes shift ΔS ($\Delta S = E_{fd} - E_{df}$).[20] From the above we obtain the following approximate relationship (see also Fig. 1b):

$$\Delta E_{5d\text{-}CB} = E_{VC} - E_{df} - E_{CT} \quad (4)$$

Here is E_{df} the energy of the 5d–4f emission of Eu^{2+} and E_{CT} the Eu^{3+} CT energy. E_{VC} is the energy difference between the top of the valence band and the bottom of the conduction band (*i.e.* the bandgap of the host lattice), which includes the exciton binding energy.[25]

The energy of the lowest relaxed 5d state is determined by the centroid shift (CS) and crystal field splitting (CFS) of the 5d levels, together with the Stokes shift. CS and CFS both decrease with increasing Eu–X distance (X = anion).[32,33] Since most compounds tend to expand with increasing temperature, resulting in larger Eu–X distances, CS and CFS both become smaller with increasing temperature, meaning that the Eu^{2+} 4f–5d energy increases with temperature. According to the Varshni equation,[34] the temperature dependency of the bandgap is given by:

$$E_{VC} = E_0 - \frac{aT^2}{b + T} \quad (5)$$

Here a and b are material constants. The Varshni equation thus shows a decrease of the bandgap with increasing temperature. So, assuming that the position of the 4f level is constant with temperature, both the increase of the 4f–5d energy and the decrease of the bandgap (*i.e.* lowering of the conduction band) with increasing temperature, will reduce the energy difference between the lowest 5d state and the bottom of the conduction ($\Delta E_{5d\text{-}CB}$). On the other hand, the Stokes shift might increase with increasing temperature, which will increase $\Delta E_{5d\text{-}CB}$.

2.3 Other causes of thermal quenching

Besides the intrinsic thermal quenching caused by either thermal ionization from the 5d to the conduction band or by direct relaxation to the ground state *via* the crossing point of the 4f and 5d parabola, other mechanisms can also cause a decrease of emission intensity with increasing temperature. One of these is temperature dependent energy transfer. Since the probability of energy transfer is likely to increase with increasing temperature, the transfer towards defects on which the Eu^{2+} 5d–4f emission is quenched, will also increase. Thermally activated concentration quenching is especially significant if the Eu^{2+} concentration is relatively high, in which case there is a lot of energy transfer between Eu^{2+} ions. In that case the thermal quenching is strongly dependent on the Eu concentration, as has been observed in for example $Sr_2Si_5N_8$:Eu^{2+}.[35] So in order to identify the intrinsic thermal quenching behaviour, the measurements have to be performed with a low activator concentration. However, concentration dependence may even occur at lower concentrations around 1%. Thermally activated concentration quenching has for example been shown to be responsible for the decrease of luminescence intensity in YAG:1%Ce^{3+} between room temperature and 600 K, even though the intrinsic quenching temperature in YAG:Ce^{3+} is well above 600 K.[36]

Another effect, which can decrease the observed emission intensity (external quantum efficiency) without decreasing the internal quantum efficiency of the phosphor, is a temperature dependency of the absorption strength. This may be due to for example a temperature dependency of the oscillator strength, or as a result of a shift of the absorption band maximum as a consequence of a temperature dependency of the centroid shift or the crystal field splitting of the 5d levels due to expansion of the host lattice at higher temperatures. Note that the absorption strength may also increase with increasing temperature, resulting in an increase of the emission intensity.

Table 1 Overview of the Eu^{2+} doped nitridosilicate phosphors for which the thermal quenching has been reported in literature. In column 2 the recorded temperature range is given; column 3 states to which category (see Fig. 2) the thermal quenching behaviour belongs; column 4 states the references from which the thermal quenching data are obtained; and column 5 states other references that present thermal quenching data

Host lattice	Temp. range (K)	Thermal quenching category	Ref. used for evaluation	Other ref.
α-Si_3N_4	298–573	2	38	—
$LiSi_2N_3$*	298–473	1	39	40
$CaSiN_2$*	293–573	3	41	—
$Ca_{16}Si_{17}N_{34}$	298–523	3	42	—
$Ca_2Si_5N_8$	295–573[a]	3	43	44–47
$SrSiN_2$	298–473	1	48	—
$Sr_2Si_5N_8$	298–573	1	43	44, 45 and 49–57
–$Sr_2Si_5N_8$	5–433	1	58	
$SrSi_6N_8$	298–573	1	6	—
$Ba_2Si_5N_8$	298–573	1	44	43–45 and 59
–$Ba_2Si_5N_8$	4–280	1	60	—
–$Ba_2Si_5N_8$	80–500	4	61	—
$BaSi_7N_{10}$	80–480	1	62	63 and 64
$BaSi_6N_8$	298–573	3	65	—
$Sr_8Mg_7Si_9N_{22}$*	298–523	1	66	—
$SrMg_3SiN_4$	4–310	3	67	68
$BaMg_3SiN_4$	4–600	3	69	—
$Li_4Ca_3Si_2N_6$	293–523	1	70	—
$Li_2CaSi_2N_4$*	298–423	1	71	—
$Li_2SrSi_2N_4$*	298–473	1	72	—
$Li_2Ca_2Mg_2Si_2N_6$	303–563	1	22	—
$SrScSi_4N_7$	293–453	1	73	—
$SrScSi_4N_7$	298–423	1	74	—
$CaYSi_4N_7$*	293–443	2	75	—
$SrYSi_4N_7$	298–523	3	76	73 and 75
$BaYSi_4N_7$*	298–443	1	75	—
$La_{2.23}Ca_{1.155}Si_6N_{11}$	4–300	3	77	—

* Thermal quenching is already severe at the lowest recorded temperature (*i.e.* room temperature). [a] Emission intensity of $Ca_2Si_5N_8$:Eu as a function of temperature has also been reported for the low temperature range (10–300 K) by Wei *et al.*[47] However, only for a very high Eu concentration ($Ca_{1.9}Eu_{0.1}Si_5N_8$).

3. Eu^{2+} absorption and emission in the nitridosilicates

3.1 Thermal quenching data of the Eu^{2+} doped nitridosilicate phosphors

Data have been collected from literature on the thermal quenching of the Eu^{2+} 5d–4f emission of all Eu^{2+} doped nitridosilicate phosphors with the general composition $M_xSi_yN_z$:Eu^{2+} (M = alkali, alkaline earth or rare earth), see Table 1. As the thermal quenching is generally strongly dependent on the Eu^{2+} concentration with a stronger thermal quenching for higher concentrated samples,[37] we have limited ourselves to samples with a low Eu^{2+} concentration. Structural information, as well as information on the optical properties of the Eu^{2+} doped nitridosilicate phosphors is reviewed in our previous publications.[25,26] For some nitridosilicate phosphors, the thermal quenching of the luminescence has been reported by various authors in multiple different publications. If there are no significant differences between the reported results, we use in this work the thermal quenching from the paper that shows the most detailed information and considers the longest temperature range, as indicated in Table 1. In case there are significant differences ($Ba_2Si_5N_8$:Eu^{2+}, $SrScSi_4N_7$:Eu^{2+}) or in case different, non-comparable temperature ranges were considered ($Sr_2Si_5N_8$:Eu^{2+}), both results are shown in Table 1. For the interest of the reader, Table 1 also lists all other references in which thermal quenching data have been published. Note that we have included, for the sake of completeness, various Mg and Li containing nitridosilicates, such as $SrMg_3SiN_4$:Eu^{2+} and $LiSi_2N_3$:Eu^{2+}, even though one may argue that some of these are not really nitridosilicates, but magneso- or litho-nitridosilicates, as Mg and Li may form MgN_4 and LiN_4 tetrahedra similar to the SiN_4 tetrahedra and can thus be considered part of the framework.

If the thermal quenching of the Eu^{2+} 5d–4f emission occurs *via* one dominating thermally activated process, the temperature dependent internal quantum efficiency can be described by the equation:[20]

$$I = \frac{I_0}{1 + C\exp\left(-\frac{E_{act}}{k_B T}\right)} \quad (6)$$

Here is T the absolute temperature, k_B the Boltzmann constant, E_{act} the activation energy for thermal quenching and I and I_0 the internal quantum efficiency at temperature T and at low temperature when there is no thermal quenching, respectively. Note that I and I_0 are normally represented by the integrated emission intensity, but this is only true in case the absorption strength is not temperature dependent. C is supposed to be a constant that is equal to the ratio between the attempt rate for thermal quenching (Γ_0) and the radiative decay rate of the 5d state of Eu^{2+} (Γ_ν).[20] Eqn (6) can be rewritten as a linear equation:

$$\ln\left(\frac{I_0}{I}-1\right)=\ln C-E_{act}\left(\frac{1}{k_BT}\right) \quad (7)$$

Hence, by fitting the thermal quenching data on an $\ln(I_0/I-1)$ *versus* $(1/k_BT)$ plot, E_{act} and C can be determined based on the slope and intercept with the y-axis, respectively. In order to plot $\ln(I_0/I-1)$ *versus* $(1/k_BT)$, the value of I_0 should be known, but for many compounds listed in Table 1, the temperature dependency of the emission intensity has not been measured down to sufficiently low temperature, *e.g.* 4 K. In case the emission intensity is constant or changing only weakly around the lowest recorded temperature, it can be assumed that the emission intensity does not change significantly down to 4 K, and I_0 can be estimated with considerable certainty. However, if the intensity is strongly changing with temperature around the lowest recorded temperature, obtaining I_0 by means of extrapolating the thermal quenching data at the low temperature side, will result in a large uncertainty. The compounds for which this is the case have been indicated with an asterisk (*) in column 1 of Table 1. Note that I_0 can also be obtained by directly fitting the thermal quenching data using eqn (6) with I_0, C and E_{act} as variables, but also in that case the variables will have a large uncertainty if thermal quenching is partly outside the recorded temperature range.

When considering an $\ln(I_0/I-1)$ *versus* $(1/k_BT)$ plot of the temperature dependent emission intensity data of the Eu^{2+} doped nitridosilicates, four different categories can be distinguished based on the shape of the curve, as illustrated in Fig. 2.

- Category 1: the data (Fig. 2a) are on a straight line, of which the slope is equal to $-E_{act}$ and the intersect with the y-axis is equal to $\ln(C)$, suggesting that the thermal quenching can be well described by eqn (6).
- Category 2: the data (Fig. 2b) are on a downward slope with an increasing gradient, *i.e.* the slope is less steep at higher temperature (small $1/k_BT$) than at lower temperature (large $1/k_BT$).
- Category 3: the data (Fig. 2c) are on a downward slope with a decreasing gradient, *i.e.* the slope is steeper at higher temperature (small $1/k_BT$) than at lower temperature (large $1/k_BT$).
- Category 4: the emission intensity initially increases with increasing temperature, giving $I_0 < I$, which cannot be displayed on an $\ln(I_0/I-1)$ *vs.* $(1/k_BT)$ plot (Fig. 2d).

As listed in Table 1, the thermal quenching behaviour of $LiSi_2N_3$:Eu^{2+}, $SrSiN_2$:Eu^{2+}, $Sr_2Si_5N_8$:Eu^{2+}, $SrSi_6N_8$:Eu^{2+}, $BaSi_7N_{10}$:Eu^{2+}, $Sr_8Mg_7Si_9N_{22}$:Eu^{2+}, $Li_2CaSi_2N_4$:Eu^{2+}, $Li_4Ca_3Si_2N_6$:Eu^{2+}, $SrScSi_4N_7$:Eu^{2+} and $BaYSi_4N_7$:Eu^{2+} belong to category 1 as the data fall (almost) on a straight line on an $\ln(I_0/I-1)$ *versus* $(1/k_BT)$ plot, while in $Li_2Ca_2Mg_2Si_2N_6$:Eu^{2+} and $Li_2SrSi_2N_4$:Eu^{2+} the data

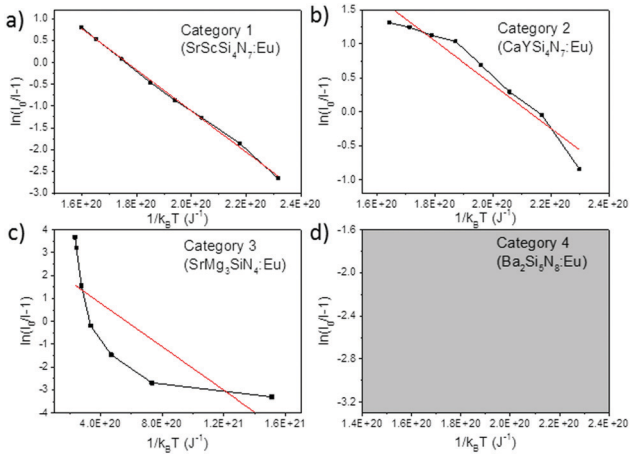

Fig. 2 Examples of the four different categories of thermal quenching on an $\ln(I_0/I-1)$ *versus* $(1/k_BT)$ plot: category 1 (linear), category 2 (downward slope with an increasing gradient), category 3 (downward slope with a decreasing gradient), and category 4 (emission intensity initially increases with increasing temperature, which cannot be displayed on an $\ln(I_0/I-1)$ *vs.* $(1/k_BT)$ plot). The black lines represent the measured data, the red lines represent the fits with eqn (7).

fluctuate around a straight line. For $CaYSi_4N_7$:Eu^{2+} and α-Si_3N_4:Eu^{2+} there is an increasing gradient with increasing $(1/T)$ (category 2), while for $CaSiN_2$:Eu^{2+}, $Ca_{16}Si_{17}N_{34}$:Eu^{2+}, $Ca_2Si_5N_8$:Eu^{2+}, $BaSi_6N_8$:Eu^{2+}, $SrMg_3SiN_4$:Eu^{2+}, $BaMg_3SiN_4$:Eu^{2+}, $SrYSi_4N_7$:Eu^{2+} and $La_{2.23}Ca_{1.155}Si_6N_{11}$:$Eu^{2+}$ there is a decreasing gradient with increasing $(1/T)$ (category 3). In the low temperature range (80–300 K) for $Ba_2Si_5N_8$:Eu^{2+} the integrated emission intensity initially increases with increasing temperature according to Wang *et al.*[61] (category 4). In contrast, Piao *et al.*[60] report a slow gradual decrease of integrated emission intensity with increasing temperature between 4 K and 280 K. For all authors, above 300 K the emission intensity decreases with increasing temperature, following approximately a linear trend on an $\ln(I_0/I-1)$ *vs.* $(1/k_BT)$ plot (*i.e.* category 1). A more detailed analysis of the thermal quenching of $Ba_2Si_5N_8$:Eu^{2+} can be found in the ESI† (Section S1.4).

3.2 Activation energy and quenching temperature

In the ESI† (Section S1) the thermal quenching of all the nitridosilicates is analysed in more detail, with regard to the four different thermal quenching categories discussed above, and the activation energy has been determined. The main conclusions from this analysis are summarized in this section.

For the nitridosilicates belonging to category 2 or 3, for which there is a deviation from a straight line on an $\ln(I_0/I-1)$ *vs.* $(1/k_BT)$ plot (Fig. 2b and c), various causes have been considered that may explain the deviation from the linear behaviour. These possible causes are: (1) a temperature dependency of the activation energy, (2) a temperature dependency of the absorption strength, (3) the presence of Eu^{2+} in different crystallographic environments with different thermal quenching behaviour, (4) temperature dependent energy transfer, and (5) the presence of secondary (anomalous) emission. In order to determine whether these possible causes can reasonably

explain the observed deviations from the linear behaviour, we have made adaptations to eqn (6) and checked whether the thermal quenching data can be well described with these adapted equations (see ESI†). From our analysis, we can conclude that the deviations from the non-linear behaviour observed for the two compounds of category 2 (α-Si_3N_4:Eu^{2+} and $CaYSi_4N_7$:Eu^{2+}) are attributed to disorder in these structures, which gives rise to Eu^{2+} ions in many slightly different crystallographic environments. Of the compounds of category 3, the non-linear quenching in $BaMg_3SiN_4$:Eu^{2+}, and possibly also $SrMg_3SiN_4$:Eu^{2+}, is caused by the presence of trapped-exciton emission. The non-linear behaviour for $Ca_2Si_5N_8$:Eu^{2+}, $Ca_{16}Si_{17}N_{34}$:Eu^{2+} and $La_{2.23}Ca_{1.155}Si_6N_{11}$:$Eu^{2+}$, which also belong to category 3, is likely due to the presence of Eu^{2+} at different crystallographic sites.

As for the nitridosilicates of thermal quenching category 1, *i.e.* the emission intensity data approximately follow a linear trend on an $\ln(I_0/I - 1)$ *vs.* $(1/k_BT)$ plot (Fig. 2a), it is noted that the value of C obtained from either fitting with eqn (6) or (7), shows large differences among the various nitridosilicates. For $Li_2Ca_2Mg_2Si_2N_6$:Eu^{2+}, $Li_4Ca_3Si_2N_6$:Eu^{2+} and $BaYSi_4N_7$:Eu^{2+} the value of C is relatively large ($>10^4$). However, for the other compounds, C is much smaller and ranges between 1 and 10^4. C is equal to the ratio of the attempt rate for thermal quenching and the radiative decay rate of the 5d–4f emission of Eu^{2+}. The first one is typically in the order of 10^{13} s^{-1},[20] while the latter one is in the order of 10^6 s^{-1},[20] giving a value of C of about 10^7. Although these rates will vary among the different hosts, it seems not realistic that C can be more than a factor 1000 smaller, *i.e.* smaller than 10^4. It was found that a temperature dependency of the absorption strength or temperature dependency of the activation energy cannot explain the unrealistically low value of C. Thermally activated concentration quenching can however not be excluded as the cause for the low value of C and is suggested to even be the main reason for the thermal quenching observed in $BaSi_7N_{10}$:Eu^{2+}. For $Sr_2Si_5N_8$:Eu^{2+}, and possibly also $Li_2CaSi_2N_4$:Eu^{2+}, $Li_2SrSi_2N_4$:Eu^{2+} and $Sr_8Mg_7Si_9N_{22}$:Eu^{2+} the presence of Eu^{2+} on different crystallographic sites, in combination with a temperature dependent energy transfer between these sites, can be assigned as the cause of the low observed value of C.

The activation energies for the intrinsic quenching of the Eu^{2+} 5d–4f emission in the nitridosilicates, as obtained from the analysis in the ESI,† are listed in Table 2. The activation energy for thermal quenching is generally below 0.5 eV. However, if the activation energy for thermal quenching is calculated with eqn (3), which is based on the model that thermal quenching occurs by direct relaxation from the 5d excited state to the 4f ground state *via* a thermally activated cross-over, a significantly higher activation energy is obtained (typically around 6 eV), see ESI,† Fig. S1b. In addition, there is no clear correlation between the activation energy and the Stokes shift. This indicates that the thermally activated cross-over model cannot be the main cause of thermal quenching in the nitridosilicates.

The quenching temperature ($T_{50\%}$) of the Eu^{2+} 5d–4f emission, *i.e.* the temperature at which half of the emission is quenched, has been determined for the nitridosilicates from literature data (see ESI†) and is shown in Table 2. Following eqn (6), $T_{50\%}$ can also be calculated from E_{act} and C:

$$T_{50\%} = \frac{E_{act}}{k_B \ln(C)} \quad (8)$$

Therefore, if there is not much variation in C among the nitridosilicates, one would expect a linear relation between the quenching temperature and the activation energy. From Fig. 3, displaying the quenching temperature *versus* the activation energy, a certain increase of the quenching temperature with

Table 2 Activation energy and quenching temperature of the intrinsic thermal quenching in the nitridosilicates, derived from experimental data from literature. See ESI for more details

Compound	E_{act} (eV)	$T_{50\%}$ (K)
α-Si_3N_4	?	>600
$LiSi_2N_3$	>0.23	~420
$CaSiN_2$	?	~390
$Ca_{16}Si_{17}N_{34}$	?	500
$Ca_2Si_5N_8$	?	460
$SrSiN_2$	>0.22	450
$Sr_2Si_5N_8$ (site 1)	0.42	600
$Sr_2Si_5N_8$ (site 2)	0.34	450
$SrSi_6N_8$	>0.25	440
$Ba_2Si_5N_8$	?	530
$BaSi_7N_{10}$	?	>600
$BaSi_6N_8$	?	510
$Sr_8Mg_7Si_9N_{22}$	>0.09	~170
$SrMg_3SiN_4$	0.28	240
$BaMg_3SiN_4$	0.46	400
$Li_4Ca_3Si_2N_6$	0.44	460
$Li_2CaSi_2N_4$	>0.17	~200
$Li_2SrSi_2N_4$	>0.12	~290
$Li_2Ca_2Mg_2Si_2N_6$	0.45	420
$SrScSi_4N_7$	>0.22	380
$CaYSi_4N_7$	?	<300
$SrYSi_4N_7$	?	460
$BaYSi_4N_7$	0.31	~370
$La_{2.23}Ca_{1.155}Si_6N_{11}$	?	260

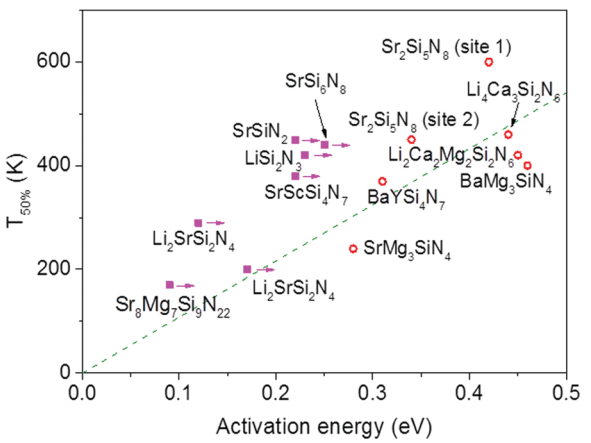

Fig. 3 Temperature at which 50% of the Eu^{2+} 5d–4f emission is quenched ($T_{50\%}$) *versus* the activation energy for thermal quenching (E_{act}) for the Eu^{2+} doped nitridosilicates. A compound is given a magenta solid square if the activation energy represents a minimum value. Other compounds are given a red open circle. See ESI† for more details. The dashed green line is a linear fit of the red data points through the origin with the equation $T_{50\%}$ (K) = 1082 × E_{act} (eV).

increasing activation energy can also be observed, but the amount of data is limited and the uncertainty of the activation energy is relatively large. By fitting the literature data through the origin, C can be determined from the slope, giving $C = 4.6 \times 10^5$, which is a reasonable value.

4. Cause of the thermal quenching and its dependence on the nitridosilicate composition

4.1 Composition dependence of the thermal quenching

In Fig. 4 the quenching temperature ($T_{50\%}$) is given as a function of the Si/N ratio. With increasing degree of condensation (Si/N ratio) the quenching temperature tends to increase. For example, $SrMg_3SiN_4$:Eu^{2+} with low Si/N ratio of 0.25 has a $T_{50\%}$ of about 200 K, while α-Si_3N_4:Eu^{2+} with high Si/N ratio of 0.75 has a $T_{50\%}$ above 600 K. The scattering is however large and $T_{50\%}$ of $LiSi_2N_3$:Eu^{2+} with relatively high Si/N ratio of 0.67 is about the same as $T_{50\%}$ of $BaMg_3SiN_4$:Eu^{2+} (about 400 K) with relatively low Si/N ratio of 0.25. In the next sections we will discuss what the mechanism is of the thermal quenching in the nitridosilicates and why there seems to be a correlation between the Si/N ratio and quenching temperature.

4.2 Thermal quenching by thermal ionization to the conduction band

If thermal ionization of the Eu^{2+} 5d electron to the host lattice conduction band is responsible for the thermal quenching of the Eu^{2+} 5d–4f emission in the nitridosilicates, one would expect a relation between the quenching temperature or activation energy at one side, and the energy difference between the lowest Eu^{2+} 5d level and the bottom of the host lattice conduction band ($\Delta E_{5d\text{-}CB}$) at the other side. Following eqn (4) in Section 2.2, $\Delta E_{5d\text{-}CB}$ can be approximated from the bandgap (E_{VC}), the Eu^{2+} 5d–4f emission energy (E_{df}) and the Eu^{3+} charge transfer energy (E_{CT}).

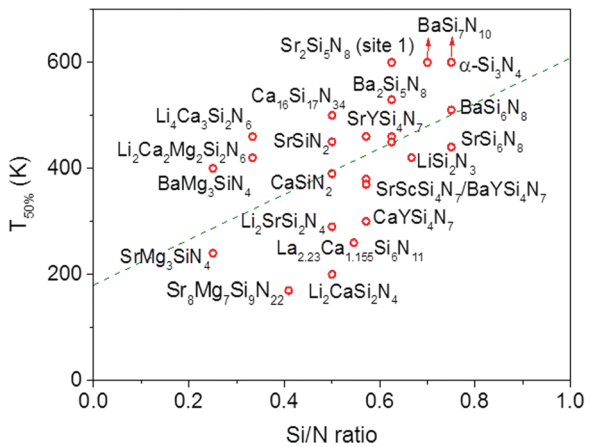

Fig. 4 Temperature at which 50% of the Eu^{2+} 5d–4f emission is quenched ($T_{50\%}$) *versus* the Si/N ratio of the Eu^{2+} doped nitridosilicates. The dashed green lines is a linear fit through the data points to indicate the trend.

The bandgap and the emission energy have been measured for many nitridosilicates, but unfortunately the energy of the Eu^{3+} CT transition cannot be measured directly for most nitridosilicates. It namely requires the presence of Eu^{3+}, while in most nitridosilicates Eu is only present in the divalent state, with the notable exception of Li_2SiN_2:Eu^{3+} [78] and $(Eu^{2+})(Eu^{3+})SiN_3$.[79] Fortunately, the Eu^{3+} CT transition in a specific nitridosilicate host lattice can be estimated based on the experimentally observed CT transitions of Sm^{3+} and Yb^{3+} in the same nitridosilicate host lattice. The CT energy of a Ln^{3+} (Ln = lanthanide) ion is namely equal to the energy difference between the top of the host lattice valence band and the 4f ground state of the corresponding divalent Ln^{2+} ion,[80] while the energy differences between the different lanthanides does not change between compounds. The Eu^{3+} CT energy can therefore be calculated from the CT transitions of Sm^{3+} or Yb^{3+}, using the fixed energy differences between the 4f ground states of Eu^{2+}, Sm^{2+} and Yb^{2+}: for every compound the Sm^{3+} CT is 1.25 eV higher in energy than the Eu^{3+} CT in the same compound, and the Yb^{3+} CT is 0.43 eV higher in energy than the Eu^{3+} CT in the same compound.[81] Using these CT transitions, $\Delta E_{5d\text{-}CB}$ can then be calculated based on eqn (4). The results are presented in Table 3.

Of the five compounds listed in Table 3, there are three compounds ($SrMg_3SiN_4$:Eu^{2+}, $Ca_2Si_5N_8$:Eu^{2+} and $Sr_2Si_5N_8$:Eu^{2+}) of which we also know the quenching temperature of the Eu^{2+} 5d–4f emission. For these three compounds the calculated $\Delta E_{5d\text{-}CB}$ has been plotted *versus* the quenching temperature (Fig. 5). As can be clearly seen, a linear relationship is observed between $\Delta E_{5d\text{-}CB}$ and the quenching temperature, as expected from eqn (8), supporting that the thermal quenching is caused by thermal activation of the Eu^{2+} 5d electron to the host lattice conduction band.

Unfortunately, the amount of nitridosilicates for which the CT energy of Eu^{3+} can be directly calculated from experimental data is very limited. However, we can make an estimation of the CT energy of Eu^{3+} for the other nitridosilicates, considering that the CT energy is determined by: (1) the distance of Eu to the neighbouring anions and (2) the nature (*i.e.* the electronegativity) of the anions involved. The Eu–N distance is determined by the size of the cation M (M = Li, Ca, Sr, Ba, La) for which Eu is substituted and can therefore be approximated by the average distance (R_{M-N}) of the metal M towards the coordinating N

Table 3 Charge transfer transitions in the rare-earth doped nitridosilicates. Column 2 shows the experimental data of the charge transfer energy of Sm^{3+}, Eu^{3+} and Yb^{3+} and column 3 shows the reference from which the CT data in column 2 has been obtained. Column 4 shows the estimated Eu^{3+} CT based on the experimental data and column 5 shows $\Delta E_{5d\text{-}CB}$ for Eu^{2+} as calculated from the Eu^{3+} CT energy (eqn (4))

Host lattice	Experimental CT (eV)	Ref.	Derived CT of Eu^{3+} (eV)	$\Delta E_{5d\text{-}CB}$ (eV)
Li_2SiN_2	3.47 (Eu^{3+})	78	3.47	[a]
$Ca_2Si_5N_8$	4.1 (Sm^{3+}), 3.3 (Yb^{3+})	82	2.87	0.43
$LaSi_3N_5$	3.1 (Yb^{3+})	83	2.67	0.03
$Sr_2Si_5N_8$ (site 1)	3.6 (Sm^{3+})	82	2.35	0.85
$SrMg_3SiN_4$	3.54 (Sm^{3+})	68	2.29	−0.19

[a] $\Delta E_{5d\text{-}CB}$ of Li_2SiN_2 cannot be calculated since E_{df} is unknown.

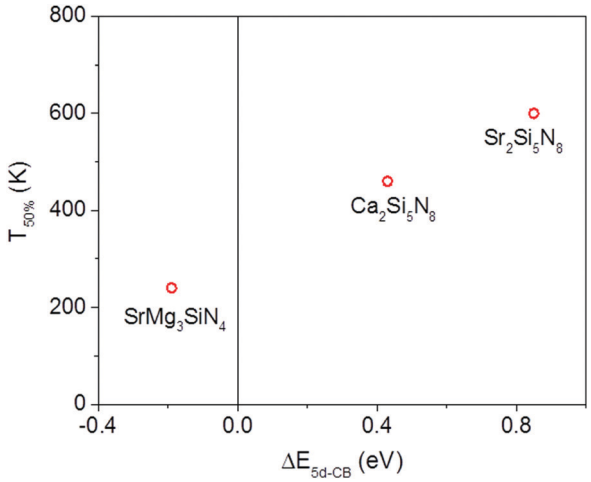

Fig. 5 Temperature at which 50% of the Eu^{2+} 5d–4f emission is quenched ($T_{50\%}$) *versus* the energy difference ($\Delta E_{5d\text{-}CB}$) between the bottom of the host lattice conduction band and the lowest relaxed Eu^{2+} 5d state for $SrMg_3SiN_4$:Eu^{2+}, $Ca_2Si_5N_8$:Eu^{2+} and $Sr_2Si_5N_8$:Eu^{2+}.

anions, which can be obtained from crystallographic data (Table 4). Since all neighbouring anions are N^{3-} anions, their electronegativity will only vary because of differences in the N by Si coordination number. As explained in our previous work,[25] the N by Si coordination number is directly proportional to the Si/N ratio (κ). Therefore, in order to estimate the Eu^{3+} CT energy of other nitridosilicates, we need to know how the CT energy depends on the average M–N distance and how it depends on the Si/N ratio. Since $Ca_2Si_5N_8$ and $Sr_2Si_5N_8$ have the same Si/N ratio, the CT energy should mainly depend on the average M–N distance. Using their CT energy (Table 3) and average $R_{M\text{–}N}$ (Table 4), the following relation is obtained:

$$E_{CT}(Eu^{3+})\ (eV) = 9.3 - 2.4R_{M\text{–}N}\ (Å) \quad \text{if } \kappa = 0.625 \qquad (9)$$

Note that a decrease of the CT energy with increasing cation size is consistent with expectations.[84,85] From eqn (9) we obtain that a hypothetical $M_2Si_5N_8$ compound with an M–N distance of 2.802 Å would have an Eu^{3+} CT energy of about 2.6 eV. The Eu^{3+} CT energy in $SrMg_3SiN_4$, which has an average M–N (= Sr–N) distance of 2.802 Å, is 2.29 eV. This gives us a second relation:

$$E_{CT}(Eu^{3+})\ (eV) = 2.1 + 0.8\kappa \quad \text{if } R_{M\text{–}N} = 2.802\ Å \qquad (10)$$

Note that we would also expect an increase of the CT energy with increasing Si/N ratio based on our previous work.[26] With increasing Si/N ratio the N by Si coordination number increases, which results in more N electrons that participate in the bonding with Si. Consequently, less N electrons are available for M–N bonding and thus also for N to Eu charge transfer, increasing the CT energy.

By combining eqn (9) and (10) the following relation is obtained for the Eu^{3+} CT energy in the nitridosilicates:

$$E_{CT}(Eu^{3+})\ (eV) = 8.8 - 2.4R_{M\text{–}N}\ (Å) + 0.8\kappa \qquad (11)$$

As a test, we can use this equation to predict the CT energy in $LaSi_3N_5$, giving 2.6 eV. This value is quite close to the actual CT energy given in Table 3: 2.67 eV. So, eqn (11) can now be used to estimate E_{CT} for the other nitridosilicates, and subsequently eqn (4) can be used to determine the energy difference between the lowest Eu^{2+} 5d state and the bottom of the conduction band of the nitridosilicate host lattice ($\Delta E_{5d\text{-}CB}$). The results are presented in Table 4.

Table 4 Average M–N distance ($R_{M\text{–}N}$), the Si/N ratio (κ), the estimated Eu^{3+} CT transition energy, and calculated energy difference between the relaxed Eu^{2+} 5d state and the bottom of the host lattice conduction band ($\Delta E_{5d\text{-}CB}$) for several nitridosilicates

Compound	$R_{M\text{–}N}$ (Å)	κ	Eu^{3+} CT (eV)	$\Delta E_{5d\text{-}CB}$ (eV)
Li_2SiN_2	2.160	0.5	3.47[a]	[a]
$LiSi_2N_3$	2.263	0.667	3.9	0.7
$CaSiN_2$	2.583	0.5	2.6	−0.3
$Ca_{16}Si_{17}N_{34}$	2.579	0.5	3.0	−0.3
$Ca_2Si_5N_8$	2.681	0.625	2.87[b]	0.4
$SrSiN_2$	2.859	0.5	2.3	0.8
$Sr_2Si_5N_8$ (site 1)	2.928	0.625	2.35[b]	0.9
$Sr_2Si_5N_8$ (site 2)	2.866	0.625	2.35[b]	0.7
$SrSi_6N_8$	3.028	0.75	2.1	−1.2
$Ba_2Si_5N_8$	2.982	0.625	2.2	0.8
$BaSi_7N_{10}$	3.287	0.7	1.5	1.7
$Sr_8Mg_7Si_9N_{22}$	2.864	0.409	2.3	−0.2
$SrMg_3SiN_4$	2.802	0.25	2.29[b]	−0.2
$BaMg_3SiN_4$	2.953	0.25	1.9	0.3
$Li_4Ca_3Si_2N_6$	2.706	0.333	2.6	−0.2
$Li_2CaSi_2N_4$	2.528	0.5	3.1	−0.2
$Li_2SrSi_2N_4$	2.722	0.5	2.7	0.1
$Li_2Ca_2Mg_2Si_2N_6$	2.588	0.333	2.9	0.0
$SrYSi_4N_7$	3.012	0.571	2.0	0.9
$BaYSi_4N_7$	3.014	0.571	2.0	0.8
$La_{2.23}Ca_{1.155}Si_6N_{11}$	2.642	0.545	2.9	−0.4

[a] $\Delta E_{5d\text{-}CB}$ of Eu^{2+} in Li_2SiN_2 cannot be determined as no Eu^{2+} 5d–4f emission has been reported for Li_2SiN_2; the Eu^{3+} CT value for Li_2SiN_2 was reported in literature. [b] Eu^{3+} CT value was derived obtained from Yb^{3+} or Sm^{3+} CT reported in literature. Other CT values have been obtained by calculation (eqn (11)).

In Fig. 6 the temperature at which 50% of the luminescence is quenched ($T_{50\%}$) is plotted *versus* $\Delta E_{5d\text{-}CB}$ for all Eu^{2+} doped nitridosilicate phosphors of Table 3. From the graph, as expected, an increase of the quenching temperature can be observed with increasing energy difference between the lowest Eu^{2+} 5d state and the bottom of the host lattice conduction band. Most of the data points follow the trend line. This again supports that the thermal ionization of the 5d electron to the conduction band is responsible for the thermal quenching in these nitridosilicates.

For $SrSi_6N_8$:Eu^{2+} the $T_{50\%}$ is much higher than expected based on the calculated $\Delta E_{5d\text{-}CB}$. The calculated $\Delta E_{5d\text{-}CB}$ is less than −1 eV, *i.e.* the lowest Eu^{2+} 5d level is positioned inside the host lattice conduction band. As a result all Eu^{2+} 5d–4f emission should actually be quenched for $SrSi_6N_8$:Eu^{2+}, even at 4 K, which obviously is not the case. Note that $SrSi_6N_8$, in which the uncommon direct Si–Si bond is present,[86] tends to deviate more often from the trends of the other nitridosilicates, having for example a smaller than expected Stokes shift for the Eu^{2+} emission,[26] and a smaller than expected bandgap than one would expect based on its Si/N ratio.[25] The low energy of the host lattice transition in $SrSi_6N_8$ has been attributed to the Si–Si bond, which forms an empty σ* state below the bottom of the

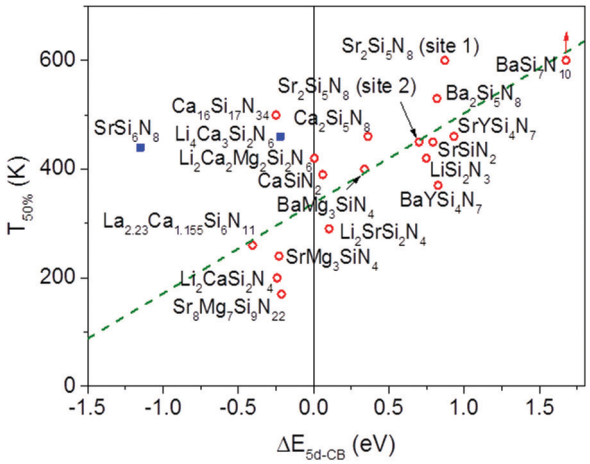

Fig. 6 Temperature at which 50% of the Eu^{2+} 5d–4f emission is quenched ($T_{50\%}$), *versus* the energy difference ($\Delta E_{5d\text{-}CB}$) between the bottom of the host lattice conduction band and the lowest Eu^{2+} 5d state. The straight green line is a linear fit through the red data points. The blue squared data points represent exceptions discussed in the text.

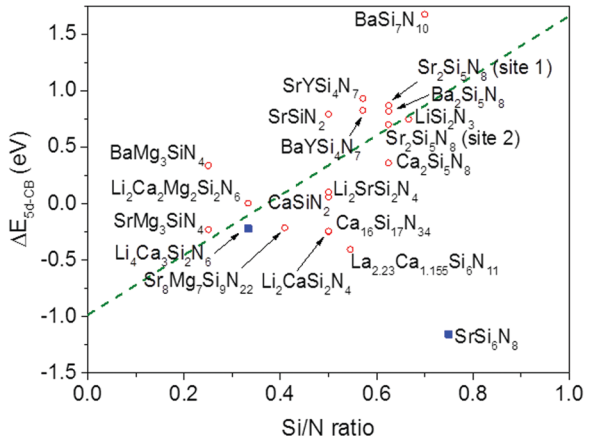

Fig. 7 $\Delta E_{5d\text{-}CB}$ *versus* the Si/N ratio in the Eu^{2+} doped nitridosilicates. The straight line is a linear fit through the red data points. The blue squared data points represent exceptions discussed in the text.

conduction band.[87] For this reason $SrSi_6N_8$:Eu^{2+} has been excluded from the fit in Fig. 6. $Li_4Ca_3Si_2N_6$:Eu^{2+} has also been excluded, because of the uncertainties in its excitation and emission spectra: the reported data suggest an extraordinary large Stokes shift of 1.76 eV,[70] which is considered very unlikely,[26] and it is more likely that the reported 5d bands have a different origin. Also for $Ca_{16}Si_{17}N_{34}$:Eu^{2+}, $La_{2.23}Ca_{1.155}Si_6N_{11}$:$Eu^{2+}$, $Sr_8Mg_7Si_9N_{22}$:Eu^{2+}, $Li_2CaSi_2N_4$:Eu^{2+} and $SrMg_3SiN_4$:Eu^{2+} a (small) negative value for $\Delta E_{5d\text{-}CB}$ has been obtained. For the latter four this is within expectation when taking into account the standard deviation, considering the fast thermal quenching of the Eu^{2+} emission in these compounds. For $Ca_{16}Si_{17}N_{34}$:Eu^{2+} $\Delta E_{5d\text{-}CB}$ seems to be too low given its relatively high quenching temperature. It might be that this deviation is related to the presence of Eu^{2+} in three different crystallographic environments in $Ca_{16}Si_{17}N_{34}$, which was not taken into account due to a lack of information about the difference in quenching behaviour for Eu^{2+} in these different crystallographic environments.

4.3 Relation between the nitridosilicate composition and $\Delta E_{5d\text{-}CB}$

From Fig. 7 one can see that there is a correlation between the degree of condensation (Si/N ratio) and $\Delta E_{5d\text{-}CB}$. $\Delta E_{5d\text{-}CB}$ tends to be small for compounds with a low Si/N ratio, such as $SrMg_3SiN_4$:Eu^{2+}, and large for compounds with a high Si/N ratio, like $BaSi_7N_{10}$:Eu^{2+}. $SrSi_6N_8$:Eu^{2+}, which is the only structure in which direct Si–Si bonds are present, is the only compound that strongly deviates from the trend. Note that the increase of $\Delta E_{5d\text{-}CB}$ with increasing Si/N ratio is in agreement with the earlier observations that $T_{50\%}$ tends to increase with Si/N ratio (Fig. 4) and that $T_{50\%}$ also increases with increasing $\Delta E_{5d\text{-}CB}$ (Fig. 6).

The increase of $\Delta E_{5d\text{-}CB}$ with increasing degree of condensation is in line with our conclusions in previous work,[25,26] in which we explained how the degree of condensation, expressed by the Si/N ratio, acts as a principle parameter that influences the structural parameters (such as bond lengths) and bandgap of the nitridosilicate lattices,[25] as well as how the degree of condensation influences 5d energy levels of the Eu^{2+} doped nitridosilicate phosphors.[26] This is illustrated in Fig. 8. With increasing Si/N ratio the N by Si coordination number increases, which results in more N electrons that participate in the bonding with Si and consequently less N electrons that are available for M–N bonding. This reduces the covalency of the M–N bonds, making them longer, while the Si–N bonds become shorter. As a consequence of the lower effective charge of N, the top of the valence band, which mainly consists of N orbitals, tends to move downward with increasing Si/N ratio, increasing the CT energy, while the bottom of the conduction band moves upward due to the decrease of the Si–N bond lengths, resulting in an overall widening of the bandgap. The lower covalency of the Eu–N bonds with increasing

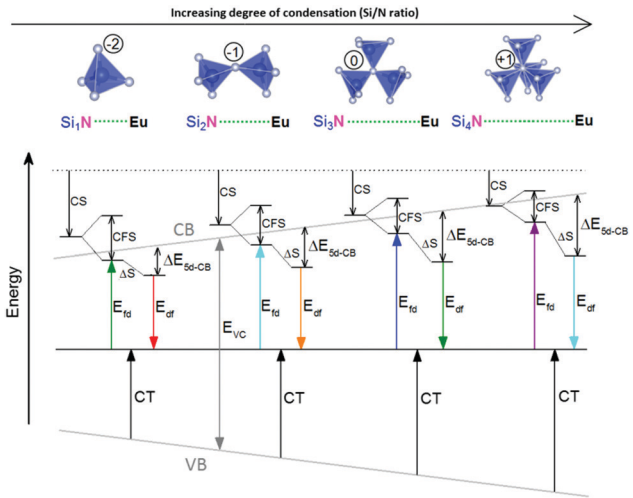

Fig. 8 Effect of the increase of the Si/N ratio on the coordination number of N with Si (NSi_x), the Eu–N bond lengths, the Eu^{2+} centroid shift (CS), the Eu^{2+} crystal field splitting (CFS), the Stokes shift of the Eu^{2+} luminescence (ΔS), the Eu^{3+} charge transfer transition (CT), $\Delta E_{5d\text{-}CB}$ of Eu^{2+} and the positions of the top of the host lattice valence band (VB) and bottom of the host lattice conduction band (CB) for the Eu^{2+} doped nitridosilicates.

Si/N ratio also weakens the nephelauxetic effect, reducing the centroid shift of the Eu^{2+} 5d levels, while the crystal field splitting of the 5d levels also becomes smaller because the Eu–N bonds become longer and the effective negative charge on N lower. The weakening of both the nephelauxetic and crystal field splitting effects result in an increase of the lowest Eu^{2+} 4f–5d absorption energy, while the Stokes shift becomes larger as the local rigidity of the Eu^{2+} sites decreases due to the longer Eu–N bonds. The consequence is that the energy difference between the relaxed 5d state and the bottom of the conduction band ($\Delta E_{5d\text{-}CB}$) will become larger with increasing Si/N ratio due to raise of the bottom of the conduction band and the increase of the Stokes shift, but that at the same time $\Delta E_{5d\text{-}CB}$ will be a bit reduced due to the decrease of the 5d redshift (which includes the nephelauxetic effect and crystal field splitting). Based on Fig. 7, that shows an increase of $\Delta E_{5d\text{-}CB}$ with increasing Si/N ratio, we can now conclude that the raise of the conduction band and increase of the Stokes shift with increasing Si/N ratio is more than compensating the reduction of the redshift. Note that we can draw this conclusion also in another way: the bandgap increases with about 4.1 eV/κ,[25] the CT increases with about 0.8 eV/κ (eqn (11)), and E_{df} increases with about 1.3 eV/κ,[26] therefore $\Delta E_{5d\text{-}CB}$ should increase with about 2 eV/κ, where κ is the Si/N ratio.

One additional issue to consider is that, in the thermal ionization to the conduction band model, the positions of the relaxed 5d level and the bottom of the conduction band are to some extent temperature dependent. With increasing temperature, as a consequence of the expansion of the lattice, a decrease of the bandgap is expected as there will be less overlap between the bonding orbitals in the valence band and the anti-bonding orbitals in the conduction band due to the longer atomic distances (Varshni equation, eqn (5)). In addition, the lowest 5d level is expected to go slightly upward in energy due to a smaller crystal field splitting as a result of the thermal expansion. Both effects are in the same direction and reinforce each other. Therefore, if one assumes that the position of the Eu^{2+} 4f ground state remains the same and that the Stokes shift does not increase (which is supported by experimental data), $\Delta E_{5d\text{-}CB}$ is expected to decrease in energy with increasing temperature as the bottom of the conduction band moves downward and the lowest 5d level moves upward. Hence, the thermal quenching will be stronger at higher temperature as $\Delta E_{5d\text{-}CB}$ (*i.e.* E_{act}) decreases, compared to what the thermal quenching would be if $\Delta E_{5d\text{-}CB}$ would remain constant. Note that eqn (6) or (7), which assume E_{act} to be constant, cannot describe any temperature dependency of $\Delta E_{5d\text{-}CB}$, consequently resulting in an error of the fitting parameters when these equations are used.

5. Conclusions and outlook

Thermal quenching of the Eu^{2+} 5d–4f emission in the nitridosilicates have been collected from literature and have been evaluated and analysed with regard to structure and composition of the nitridosilicates. According to the presented relationships, the main cause of thermal quenching of the Eu^{2+} 5d–4f emission in the nitridosilicates is the thermal ionization of the Eu^{2+} 5d electron to the host lattice conduction band, as is supported by the increase of quenching temperature ($T_{50\%}$) with increasing energy difference between the relaxed 5d state and the bottom of the conduction band ($\Delta E_{5d\text{-}CB}$). In addition, $\Delta E_{5d\text{-}CB}$ tends to increase with increasing degree of condensation (Si/N ratio) because the combined effect of the raise of the conduction band and increase of the Stokes shift with increasing degree of condensation is stronger than the decrease of redshift of the 5d levels. The weaker thermal quenching with increasing degree of condensation can thus be understood based on the interpretation described above and cannot be attributed to a more rigid structure, as is often done in literature using the configurational coordinate model.

Besides the intrinsic quenching of the emission due to thermal ionization, other effects seem to further reduce the emission intensity with increasing temperature in many nitridosilicates. These effects include quenching at defects by energy transfer, which becomes stronger at higher Eu^{2+} concentrations, and the quenching of anomalous emission.

It was found that for many compounds, even though the thermal quenching of the Eu^{2+} emission could be well fitted with an Arrhenius type of equation (eqn (6) or (7)), the obtained value of C, representing the ratio of the attempt rate for thermal quenching over the radiative decay rate of the 5d–4f emission, is unrealistically low. This raises the question whether one can trust the obtained value for the activation energy. In literature however, this low value of C is usually neither discussed nor reported. Future research should therefore focus on obtaining a better understanding of the cause of the low value of C and whether the Arrhenius type of equation is actually a good description of the full thermal quenching behaviour in these compounds.

Although this work was focussed on the quenching of the Eu^{2+} 5d–4f emission in the nitridosilicates, it is believed that the conclusions are more general and would also apply for the thermal quenching of the 5d–4f emission of other lanthanides such as Ce^{3+} or Yb^{2+}. In addition, other host lattices that consist of cross-linked TX_4 tetrahedra (T = cation, X = anion) with M cations in between, such as oxo-silicates, phosphates and aluminates, are expected to show similar relationships.

Conflicts of interest

There are no conflicts to declare.

Acknowledgements

This research has received funding from the Netherlands Organisation for Scientific Research (NWO) as part of the Joint Research Project on Advanced Materials with the National Natural Science Foundation of China (NSFC). We acknowledge the valuable input given by Prof. Dr Pieter Dorenbos during the preparation of this manuscript.

Notes and references

1 G. Li, Y. Tian, Y. Zhao and J. Lin, *Chem. Soc. Rev.*, 2015, **44**, 8688–8713.
2 Z. Xia, Z. Xu, M. Chen and Q. Liu, *Dalton Trans.*, 2016, **45**, 11214–11232.
3 J. Meyer and F. Tappe, *Adv. Opt. Mater.*, 2015, **3**, 424–430.
4 N. C. George, K. A. Denault and R. Seshadri, *Annu. Rev. Mater. Res.*, 2013, **43**, 481–501.
5 L. Wang, R.-J. Xie, T. Suehiro, T. Takeda and N. Hirosaki, *Chem. Rev.*, 2018, **118**, 1951–2009.
6 K. Shioi, N. Hirosaki, R. J. Xie, T. Takeda and Y. Q. Li, *J. Mater. Sci.*, 2008, **43**, 5659–5661.
7 K. Uheda, H. Takizawa, T. Endo, H. Yamane, M. Shimada, C. M. Wang and M. Mitomo, *J. Lumin.*, 2000, **87–89**, 967–969.
8 Y. Q. Li, C. M. Fang, G. de With and H. T. Hintzen, *J. Solid State Chem.*, 2004, **177**, 4687–4694.
9 C. J. Duan, X. J. Wang, W. M. Otten, A. C. A. Delsing, J. T. Zhao and H. T. Hintzen, *Chem. Mater.*, 2008, **20**, 1597–1605.
10 K. Uheda, N. Hirosaki, Y. Yamamoto, A. Naito, T. Nakajima and H. Yamamoto, *Electrochem. Solid-State Lett.*, 2006, **9**, H22–H25.
11 Y. Q. Li, A. C. A. Delsing, G. de With and H. T. Hintzen, *Chem. Mater.*, 2005, **17**, 3242–3248.
12 J. W. H. van Krevel, J. W. T. van Rutten, H. Mandal, H. T. Hintzen and R. Metselaar, *J. Solid State Chem.*, 2002, **165**, 19–24.
13 R. J. Xie, M. Mitomo, K. Uheda, F. F. Xu and Y. Akimune, *J. Am. Ceram. Soc.*, 2002, **85**, 1229–1234.
14 N. Hirosaki, R. J. Xie, K. Kimoto, T. Sekiguchi, Y. Yamamoto, T. Suehiro and M. Mitomo, *Appl. Phys. Lett.*, 2005, **86**, 211905.
15 J. Qiao, J. Zhao, Q. Liu and Z. Xia, *J. Rare Earths*, 2019, DOI: 10.1016/j.jre.2018.11.001.
16 Y. H. Kim, P. Arunkumar, B. Y. Kim, S. Unithrattil, E. Kim, S.-H. Moon, J. Y. Hyun, K. H. Kim, D. Lee and J.-S. Lee, *Nat. Mater.*, 2017, **16**, 543.
17 C. W. Yeh, W. T. Chen, R. S. Liu, S. F. Hu, H. S. Sheu, J. M. Chen and H. T. Hintzen, *J. Am. Chem. Soc.*, 2012, **134**, 14108–14117.
18 C. Struck and W. Fonger, *J. Lumin.*, 1975, **10**, 1–30.
19 K. Bleijenberg and G. Blasse, *J. Solid State Chem.*, 1979, **28**, 303–307.
20 P. Dorenbos, *J. Phys.: Condens. Matter*, 2005, **17**, 8103–8111.
21 Y. Fukuda, *ECS J. Solid State Sci. Technol.*, 2017, **6**, R69–R74.
22 T. M. Tolhurst, P. Strobel, P. J. Schmidt, W. Schnick and A. Moewes, *Chem. Mater.*, 2017, **29**, 7976–7983.
23 Y. Wang, J. Ding, Y. Wang, X. Zhou, Y. Cao, B. Ma, J. Li, X. Wang, T. Seto and Z. Zhao, *J. Mater. Chem. C*, 2019, **7**, 1792–1820.
24 S. Yan, *Opt. Mater.*, 2018, **79**, 172–185.
25 O. M. ten Kate, Z. Zhang and H. T. Hintzen, *J. Mater. Chem. C*, 2017, **5**, 11504–11514.
26 O. M. ten Kate, Z. Zhang, J. R. van Ommen and H. T. Hintzen, *J. Mater. Chem. C*, 2018, **6**, 5671–5683.
27 G. Blasse, *Mater. Chem. Phys.*, 1987, **16**, 201–236.
28 A. Alias, Y. Yaacob, Z. Zabidi, S. Alshurdin and N. Aini, *J. Fundam. Appl. Sci.*, 2017, **9**, 568.
29 M. Ando and Y. A. Ono, *J. Cryst. Growth*, 1992, **117**, 969–974.
30 E. Van der Kolk, J. De Haas, A. Bos, C. Van Eijk and P. Dorenbos, *J. Appl. Phys.*, 2007, **101**, 083703.
31 P. Dorenbos, *J. Phys.: Condens. Matter.*, 2003, **15**, 8417–8434.
32 P. Dorenbos, *Phys. Rev. B: Condens. Matter Mater. Phys.*, 2000, **62**, 15640–15649.
33 P. Dorenbos, *J. Alloys Compd.*, 2002, **341**, 156–159.
34 Y. P. Varshni, *Physica*, 1967, **34**, 149–154.
35 Y. Q. Li, J. E. J. van Steen, J. W. H. van Krevel, G. Botty, A. C. A. Delsing, F. J. DiSalvo, G. de With and H. T. Hintzen, *J. Alloys Compd.*, 2006, **417**, 273–279.
36 V. Bachmann, C. Ronda and A. Meijerink, *Chem. Mater.*, 2009, **21**, 2077–2084.
37 Y. Q. Li and H. Hintzen, *J. Light Visual Environ.*, 2008, **32**, 129–134.
38 Y. Q. Li, N. Hirosaki, R. J. Xie, T. Takeda and M. Mitomo, *J. Lumin.*, 2010, **130**, 1147–1153.
39 Q. S. Wu, Y. Y. Li, X. C. Wang, Z. Y. Zhao, C. Wang, H. Li, A. J. Mao and Y. H. Wang, *RSC Adv.*, 2014, **4**, 39030–39036.
40 Y. Q. Li, N. Hirosaki, R. J. Xie, T. Takeka and M. Mitomo, *J. Solid State Chem.*, 2009, **182**, 301–311.
41 Y. Q. Li, N. Hirosaki, R. J. Xie, T. Takada, Y. Yamamoto, M. Mitomo and K. Shioi, *Int. J. Appl. Ceram. Technol.*, 2010, **7**, 787–802.
42 H. Chen, J. Ding, X. Ding, X. Wang, Y. Cao, Z. Zhao and Y. Wang, *Inorg. Chem.*, 2017, **56**, 10904–10913.
43 W. T. Chen, H. S. Sheu, R. S. Liu and J. P. Attfield, *J. Am. Chem. Soc.*, 2012, **134**, 8022–8025.
44 H. L. Li, R. J. Xie, N. Hirosaki, T. Takeda and G. H. Zhou, *Int. J. Appl. Ceram. Technol.*, 2009, **6**, 459–464.
45 Y. Q. Li, G. De With and H. T. Hintzen, *J. Solid State Chem.*, 2008, **181**, 515–524.
46 C. Wang, Z. Y. Zhao, X. C. Wang, Y. Y. Li, Q. S. Wu and Y. H. Wang, *RSC Adv.*, 2014, **4**, 55388–55393.
47 X. D. Wei, L. Y. Cai, F. C. Lu, X. L. Chen, X. Y. Chen and Q. L. Liu, *Chin. Phys. B*, 2009, **18**, 3555–3562.
48 L. Chen, R. H. Liu, W. D. Zhuang, Y. H. Liu, Y. S. Hu, X. L. Ma and B. Hu, *J. Rare Earths*, 2016, **34**, 30–35.
49 R. J. Xie, N. Hirosaki, N. Kimura, K. Sakuma and M. Mitomo, *Appl. Phys. Lett.*, 2007, **90**, 191101.
50 L. Chen, R. H. Liu, W. D. Zhuang, Y. H. Liu, Y. S. Hu, X. F. Zhou, W. Gao and X. L. Ma, *CrystEngComm*, 2015, **17**, 3687–3694.
51 Y. Liu, L. Chen, X. Zhou, R. Liu and W. Zhuang, *J. Solid State Chem.*, 2017, **246**, 145–149.
52 C. C. Lin, Y.-T. Tsai, H. E. Johnston, M.-H. Fang, F. Yu, W. Zhou, P. S. Whitfield, Y. Li, J. Wang and R.-S. Liu, *J. Am. Chem. Soc.*, 2017, **139**, 11766–11770.
53 H. Yuan, Z. Huang, F. Chen, Q. Shen and L. Zhang, *J. Alloys Compd.*, 2017, **720**, 521–528.
54 V. D. Luong, W. T. Zhang and H. R. Lee, *Adv. Mater. Res.*, 2011, **233–235**, 2705–2709.
55 T. Wang, P. Zheng, X. L. Liu, H. F. Chen, L. Bian and Q. L. Liu, *J. Lumin.*, 2014, **147**, 173–178.

56 C. Wang, S. Y. Xin, X. C. Wang, G. Zhu, Q. S. Wu and Y. H. Wang, *New J. Chem.*, 2015, **39**, 6958–6964.
57 X. Q. Piao, K. Machida, T. Horikawa and B. G. Yun, *J. Lumin.*, 2010, **130**, 8–12.
58 X. Q. Piao, T. Horikawa, H. Hanzawa and K. Machida, *Appl. Phys. Lett.*, 2006, **88**, 161908.
59 J. M. Song, J. S. Park and S. Nahm, *Ceram. Int.*, 2013, **39**, 2845–2850.
60 X. Piao, K. I. Machida, T. Horikawa and H. Hanzawa, *Appl. Phys. Lett.*, 2007, **91**, 041908.
61 J. Wang, H. Zhang, Y. Liu, H. Dong, B. Lei, M. Zheng, Y. Xiao, M. Peng and J. Wang, *J. Mater. Chem. C*, 2015, **3**, 9572–9579.
62 J. L. Qin, H. R. Zhang, B. F. Lei, H. W. Dong, Y. L. Liu, J. X. Meng, M. T. Zheng and Y. Xiao, *J. Lumin.*, 2014, **152**, 230–233.
63 H. L. Li, R. J. Xie, G. H. Zhou, N. Hirosaki and Z. O. Sun, *J. Electrochem. Soc.*, 2010, **157**, J251–J255.
64 G. Anoop, D. W. Lee, D. W. Suh, S. L. Wu, K. M. Ok and J. S. Yoo, *J. Mater. Chem. C*, 2013, **1**, 4705–4712.
65 K. Ueda, H. Yamane, T. Nagura and T. Miyazaki, *Japanese Pat.*, JP2015-196717, 2015.
66 C. Li, H. W. Zheng, H. W. Wei, J. Su, F. H. Liao, Z. Y. Zhang, L. Xu, Z. P. Yang, X. M. Wang and H. Jiao, *Chem. Commun.*, 2018, **54**, 11598–11601.
67 T. M. Tolhurst, S. Schmiechen, P. Pust, P. J. Schmidt, W. Schnick and A. Moewes, *Adv. Opt. Mater.*, 2016, **4**, 584–591.
68 D. Cui, Z. Song, Z. Xia and Q. Liu, *Inorg. Chem.*, 2017, **56**, 11837–11844.
69 S. Schmiechen, P. Strobel, C. Hecht, T. Reith, M. Siegert, P. J. Schmidt, P. Huppertz, D. Wiechert and W. Schnick, *Chem. Mater.*, 2015, **27**, 1780–1785.
70 Q. Wu, J. Ding, Y. Li, X. Wang and Y. Wang, *J. Lumin.*, 2017, **186**, 144–151.
71 Q. Wu and J. Zhou, *Dyes Pigm.*, 2019, **161**, 324–330.
72 Q. Wu, Y. Li, C. Wang and J. Luo, *J. Lumin.*, 2018, **201**, 485–492.
73 T. Horikawa, M. Fujitani, H. Hanzawa and K.-I. Machida, *ECS J. Solid State Sci. Technol.*, 2012, **1**, R113–R118.
74 D. Porob, N. Karkada, N. P. Kumar and A. Setlur, *ECS Trans.*, 2012, **41**, 27–38.
75 T. Kurushima, G. Gundiah, Y. Shimomura, M. Mikami, N. Kijima and A. K. Cheetham, *J. Electrochem. Soc.*, 2010, **157**, J64–J68.
76 X. C. Wang, T. Seto, Z. Y. Zhao, Y. Y. Li, Q. S. Wu, H. Li and Y. H. Wang, *J. Mater. Chem. C*, 2014, **2**, 4476–4481.
77 C. Maak, D. Durach, C. Martiny, P. J. Schmidt and W. Schnick, *Chem. Mater.*, 2018, **30**, 3552–3558.
78 J. Y. Ding, Y. Y. Li, Q. S. Wu, Q. Long, C. Wang and Y. H. Wang, *J. Mater. Chem. C*, 2015, **3**, 8542–8549.
79 M. Zeuner, S. Pagano, P. Matthes, D. Bichler, D. Johrendt, T. Harmening, R. Pöttgen and W. Schnick, *J. Am. Chem. Soc.*, 2009, **131**, 11242–11248.
80 P. Dorenbos, *J. Alloys Compd.*, 2009, **488**, 568–573.
81 P. Dorenbos, *ECS J. Solid State Sci. Technol.*, 2013, **2**, R3001.
82 O. M. ten Kate, Z. Zhang, P. Dorenbos, H. T. Hintzen and E. van der Kolk, *J. Solid State Chem.*, 2013, **197**, 209–217.
83 O. M. ten Kate, H. T. Hintzen, P. Dorenbos and E. van der Kolk, *J. Mater. Chem.*, 2011, **21**, 18289–18294.
84 H. Hoefdraad, *J. Solid State Chem.*, 1975, **15**, 175–177.
85 P. Dorenbos, *J. Lumin.*, 2005, **111**, 89–104.
86 F. Stadler, O. Oeckler, J. Senker, H. A. Höppe, P. Kroll and W. Schnick, *Angew. Chem., Int. Ed.*, 2005, **44**, 567–570.
87 Z. Huang, F. Chen, J. Zhang, Q. Shen and L. Zhang, *RSC Adv.*, 2017, **7**, 8779–8785.